Validation of a Faulted Rotor Induction Machine Model With an Insightful Geometrical Interpretation of Physical Quantities

Carlo Concari, *Member, IEEE*, Giovanni Franceschini, Carla Tassoni, *Senior Member, IEEE*, and Andrea Toscani

***Abstract*—Many proposals about induction-machine broken-bar detection can be found in the literature. Disturbances that affect phase currents, current space vector, power, fluxes, torque, and speed have been utilized to diagnose mains-supplied machines. Nevertheless, there is still disagreement about how the fault signatures of the different variables correlate with the actual fault and how they depend on the operating conditions. This paper presents a simple but effective analytical representation of induction machines with rotor faults, based on a synchronous reference frame and on Steinmetz's phasors. The developed relationships can be visualized through equivalent circuits, feedback loop block diagrams, or geometrical loci, allowing a deep understanding of the underlying physical phenomena, particularly as functions of inertia and of the machine parameters. The insight thus gained helps to enhance the quantification of fault severity with respect to the usual diagnostic technique based on the sum of the sidebands, clearly defining for the first time the field of validity of such technique. The analytical results are verified through simulations and experiments.**

***Index Terms*—Analytical model, broken bars, condition monitoring, fault diagnosis, induction machines, inverse problems, modeling, motor current signature analysis (MCSA), spectral analysis.**

NOMENCLATURE

t	Time.
ω	Supply pulsation.
s	Slip.
v	Supply voltage.
i	Phase current.
λ	Magnetic flux linkage.
I, Φ	Amplitude, angle of fundamental stator current.
i_0	Magnetizing current.
e	Electromotive force (EMF).
R	Phase resistance.
l, M	Leakage, magnetizing inductance.
P	Number of pole pairs.
k	Harmonic order of disturbance.
J, J_v	Motor-load combined inertia, virtual inertia.
K_T, K_P^{ω}	Brake machine constant, speed loop proportional gain.
N, n	Total rotor bars, contiguous broken rotor bars.
N_s	Number of stator turns per equivalent circuit.
p	Differential operator d/dt.
ω_r	Mechanical rotor pulsation.
θ	Mechanical rotor angle.
T_{em}	Electromagnetic (EM) torque.
x, X_m	Leakage, magnetizing reactance at supply pulsation.
$\overline{Z}$	Specific machine impedance seen by fault-induced EMF.
δ	Adjacent rotor bars displacement.
i_l, i_r	Left, right current sideband component.
i_l'	Left current sideband component when $J \to \infty$.
i_l''	Left current sideband component due to speed ripple.
$\Delta T_{\mathrm{em}}'$	EM torque ripple when $J \to \infty$.
$i_{\mathrm{act}}, i_{\mathrm{react}}$	Active, reactive component of stator current.
$i_{\mathrm{stat}}, i_{\mathrm{rot}}$	Stator, rotor current ripple caused by fault-induced EMF.
ψ	Angle between $\overline{\Delta I}_{\mathrm{act}}$ and $-j\overline{\Delta I}_{\mathrm{react}}$.
β	Angle between $\overline{\Delta I}_{\mathrm{act}}$ and $\overline{I}_r$.
α	Angle between $\overline{I}_r$ and fault-induced EMF.

Subscripts

d, q	Healthy, faulty axis of faulty rotor.
s, r	Stator, rotor quantity.
b, e	Rotor bar, end ring quantity.
p, n	Positive, negative sequence symmetrical component.

Modifiers

Δx	Fault-induced ripple of quantity x.
$\overline{X}$	Steinmetz's representing phasor of quantity x.
$\vec{x}$	Space vector of quantity x.
X	Amplitude of quantity x.
φ_x	Phase angle of quantity x.

All the rotor quantities are referred to the stator.

I. INTRODUCTION

As FAR as electric rotor faults in induction motors are concerned, different physical quantities present anomalies that can be used to detect the fault event: Currents, torque, speed, and magnetic flux all contain fault-dependent spectral components [1]. Historically, researchers have chosen mainly

Manuscript received March 30, 2012; revised June 26, 2012 and August 31, 2012; accepted November 7, 2012. Date of publication November 19, 2012; date of current version May 2, 2013.

The authors are with the Department of Information Engineering, University of Parma, 43124 Parma, Italy (e-mail: carlo.concari@unipr.it; giovanni.franceschini@unipr.it; carla.tassoni@unipr.it; andrea.toscani@unipr.it).

Color versions of one or more of the figures in this paper are available online at http://ieeexplore.ieee.org.

Digital Object Identifier 10.1109/TIE.2012.2228142

to use phase currents [a technique known as motor current signature analysis (MCSA)] which can be monitored cheaply and practically.

In case of mains-supplied motors, the amplitude of the phase current component at $(1 - 2s)\omega$ at first [2] and, some years later, the amplitude of both sidebands at $(1 \pm 2s)\omega$ [3] have been proposed as fault indexes to quantify the fault severity. Many researchers followed and modified these approaches [4]–[8], with the aim of improving the efficiency of the diagnostic procedure.

In recent years, the problems arising from converter supply noise, the presence of different types of control, and, overall, time-varying conditions have oriented the researchers toward advanced digital signal processing and artificial intelligence. In this context, the quantification of the fault, or at least the determination of an alarm threshold justified through the physical behavior of the faulty machine, has become secondary issues. An attempt to link the machine reaction to the fault-induced speed modulation was presented in [3], in which the focal point was determining how to combine the amplitudes of the two current sidebands. In this paper, the underlying assumptions were not fully supported; moreover, computing phase displacement by fast Fourier transform is not effective, and the results were not convincing.

Some authors tried to overcome this problem by considering a modulation index and distinguishing between phase and amplitude modulation [9]–[13], considering the envelope of the current signal [14], [15], or introducing unjustified assumptions about the phase displacement [8]. The influence of the motor-load combined inertia on this displacement was never addressed. Only paper [16], through the so-called "Vienna monitoring system," gives results independent of inertia, but the proposed method needs voltage, current, and speed signals and requires heavy computations while not providing a fault severity diagnosis.

Some improvements have been introduced considering the power signal or, in case of mains-supplied machines, the current space vector. Through the active and reactive components at $2s\omega$, researchers tried to obtain further indications to diagnostic aims [17]–[20]. The question of how rotor faults or load oscillations influence these signals produced many papers aimed at distinguishing between the two events [10], [21]–[24].

The authors have presented a procedure to correlate the Steinmetz phasors of phase current sideband components with the phasors of active and reactive current space vector components and, therefore, to compute the unknown displacement between the sidebands, which depends largely on inertia [24]. This first step can help improve the comprehension of the underlying physical phenomena.

With the aim of finding possible correlations among the components of the different physical quantities (phase current, current space vector, torque, and speed), many simulations were performed varying inertia, load, and machine size.

The simulation results allow the authors to highlight the links among the variables. Specifically, an equivalent circuit has been developed to represent the machine reaction to the initial torque ripple due to the rotor fault at infinite inertia, i.e., at constant speed (the so-called steady state).

This new circuit, together with the well-known steady-state equivalent circuit, allows an insightful interpretation of the different phenomena involved. They can be visualized by geometrical loci plotted through the links among torque ripple, speed ripple, and current components determined with variable inertia. The main machine parameters involved are further evidenced through the variation of these loci with load and machine size. Experiments confirm the validity of the developed model.

This paper is structured as follows. Section II recalls several models proposed to simulate the machine behavior in case of broken bars. In Section III, the steady-state condition is presented, and the various assumptions that allow introducing a simple cause/effect relationship are highlighted. Speed reaction is considered in Section IV, and the mechanism that leads to the two current sidebands is described by a feedback loop scheme. The loci of current components with varying inertia are presented in Section V, as well as the influence of load and machine size. The experimental test bed is described in Section VI, while Section VII concludes this paper with the final remarks.

II. WHICH MODEL FOR INDUCTION MACHINES WITH BROKEN ROTOR BARS?

A lot of models can be found in the literature to simulate induction machines considering stator and rotor winding distributions, supply voltage waveforms, skew, and saturation [1], [25]–[33]. These models can be used to simulate any effect produced by spatial and temporal harmonics, but they cannot solve the inverse problem of determining the causes from the effects (fault quantification). Moreover, they need many machine design parameters and are not suited for highlighting the parameters that mainly influence the machine response. With fault quantification among our goals, we need a simpler model.

Let us model the machine with an ideal two-phase symmetrical stator and a rotor with $N + 1$ meshes with infinite impedance parameters in some of the branches [34]. This model, which excludes magnetic saturation and interbar currents, is suitable for calculating currents, torque, and speed with the only effects due to broken bars, i.e., the spectrum line chain at pulsations $(1 \pm 2ks)\omega$ for the currents and $\pm 2ks\omega$ for torque and speed.

Considering a small fault (one broken bar), the spectral chain can be interrupted at first order $(k = 1)$. With these premises, the machine shows a quasi-steady-state behavior characterized by a constant average value of current space vector (and of phase currents if a synchronous reference frame is used), torque, and speed, while the superimposed ripples can be considered as monoharmonic signals at pulsation $2s\omega$.

Simulations show that a two-phase rotor dynamical model with suitable asymmetry factors gives results similar to the mesh model [5], [35]–[40]. In particular, in [5], the asymmetry coefficients are linked to the rotor bar number as recalled in the following. The Park model of the machine with the asymmetrical rotor, in a reference frame rotating at the electrical rotor speed pulsation $P\omega_r$, is defined as (1), shown at the bottom of the page.

This model can be used, together with the mechanical equations, to describe the operation of the faulty rotor machine with regard only to the sideband components and their harmonics due to a rotor asymmetry.

Some simplifying assumptions can be adopted for the slip up to the rated value, with the rotor resistances being the main parameters: The difference between the $d{-}q$ linking and leakage fluxes can be neglected, while for the rotor resistances, the following relationships are adopted. If n contiguous bars are broken and axis q is oriented in the direction of the fault, the two equivalent rotor circuits have respectively $N/2$ and $(N/2-n)$ bars; therefore

$$R_{rd}=R_r=\frac{(2N_s)^2}{\frac{N}{2}}\left(R_b+\frac{\frac{R_e}{N}}{2\sin^2\left(\frac{\delta}{2}\right)}\right) \tag{2}$$

and for the faulty phase

$$R_{rq}=\frac{(2N_s)^2}{N/2-n}\left(R_b+\frac{\frac{R_e}{N}}{2\sin^2\left(\frac{\delta}{2}\right)}\right). \tag{3}$$

This simplified model was extensively tested through simulations and experiments, obtaining good results [5].

III. MACHINE BEHAVIOR WITHOUT SPEED REACTION

Instantaneous symmetrical components are suitable for the development of equivalent circuits for asymmetrical machines. Using the common mode and differential parameter system (1), with the adopted simplifying assumptions, results in (4), shown at the bottom of the page.

The difference between the two resistances referred to the healthy resistance, in case of $n \ll N$, is

$$\Delta R_r=\left[\frac{1}{N/2-n}-\frac{1}{\frac{N}{2}}\right]R_r\simeq\frac{2n}{N}R_r \tag{5}$$

and their average is $R_r+\Delta R_r/2\simeq R_r$.

Now, we proceed considering the machine behavior at constant speed, i.e., in the absence of speed reaction to the torque ripple. In this situation, considering a low severity fault, the stator current is a simple superposition of a disturbance at pulsation $(1-2s)\omega$ on the sinusoidal current at supply pulsation.

With reference to steady-state conditions, the Laplace operator p in system (4) can be replaced by $js\omega$ [35], obtaining the so-called forward–backward monoharmonic model suitable for computing the stator component at $(1-2s)\omega$. The current $\overline{I}_{sp}$ (or positive sequence) has the supply pulsation ω, and $\overline{I}_{rp}$ and $\overline{I}_{rn}$ have pulsations $s\omega$ and $-s\omega$, respectively, while $\overline{I}_{sn}$ has the pulsation $(1-2s)\omega$. We obtain (6), shown at the bottom of the page.

Normalizing the system to the supply pulsation, the system becomes (7), shown at the bottom of the next page.

It is convenient to emphasize the forward $(\overline{I}_{sn}+\overline{I}_{rn})$ and backward $(\overline{I}_{sp}+\overline{I}_{rp})$ magnetizing currents

$$\begin{aligned}
\overline{V}&=(R_s+jx_s)\overline{I}_{sp}+jX_m(\overline{I}_{sp}+\overline{I}_{rp})\\
0&=\left(\frac{R_s}{2s-1}+jx_s\right)\overline{I}_{sn}+jX_m(\overline{I}_{sn}+\overline{I}_{rn})\\
0&=jX_m(\overline{I}_{sp}+\overline{I}_{rp})+\left[\frac{R_r}{s}+jx_r\right]\overline{I}_{rp}+\frac{\frac{\Delta R_r}{2}}{s}(\overline{I}_{rp}+\overline{I}_{rn})\\
0&=jX_m(\overline{I}_{sn}+\overline{I}_{rn})+\left[\frac{R_r}{s}+jx_r\right]\overline{I}_{rn}+\frac{\frac{\Delta R_r}{2}}{s}(\overline{I}_{rp}+\overline{I}_{rn}).
\end{aligned} \tag{8}$$

$$\begin{bmatrix} v_d\\ v_q\\ 0\\ 0\end{bmatrix}=\begin{bmatrix} R_s+p(l_s+M_d) & -P\omega_r(l_s+M_q) & pM_d & -P\omega_rM_q\\ P\omega_r(l_s+M_d) & R_s+p(l_s+M_q) & P\omega_rM_d & pM_q\\ pM_d & 0 & R_{rd}+p(l_{rd}+M_d) & 0\\ 0 & pM_q & 0 & R_{rq}+p(l_{rq}+M_q)\end{bmatrix}\begin{bmatrix} i_{sd}\\ i_{sq}\\ i_{rd}\\ i_{rq}\end{bmatrix} \tag{1}$$

$$\begin{bmatrix} v_p\\ v_n\\ 0\\ 0\end{bmatrix}=\begin{bmatrix} R_s+(p+jP\omega_r)(l_s+M) & 0 & (p+jP\omega_r)M & 0\\ 0 & R_s+(p-jP\omega_r)(l_s+M) & 0 & (p-jP\omega_r)M\\ pM & 0 & R_r+p(l_r+M) & \frac{\Delta R_r}{2}\\ 0 & pM & \frac{\Delta R_r}{2} & R_r+p(l_r+M)\end{bmatrix}\begin{bmatrix} i_{sp}\\ i_{sn}\\ i_{rp}\\ i_{rn}\end{bmatrix} \tag{4}$$

$$\begin{bmatrix} \bar{V}\\ 0\\ 0\\ 0\end{bmatrix}=\begin{bmatrix} R_s+j\omega(l_s+M) & 0 & j\omega M & 0\\ 0 & R_s+j[2s-1]\omega M & 0 & j[2s-1]\omega M\\ js\omega M & 0 & R_r+js\omega(l_r+M) & \frac{\Delta R_r}{2}\\ 0 & js\omega M & \frac{\Delta R_r}{2} & R_r+js\omega(l_r+M)\end{bmatrix}\begin{bmatrix} \overline{I_{sp}}\\ \overline{I_{sn}}\\ \overline{I_{rp}}\\ \overline{I_{rn}}\end{bmatrix} \tag{6}$$

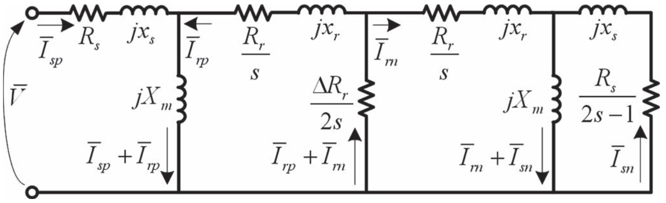

Fig. 1. Equivalent circuit corresponding to system (8).

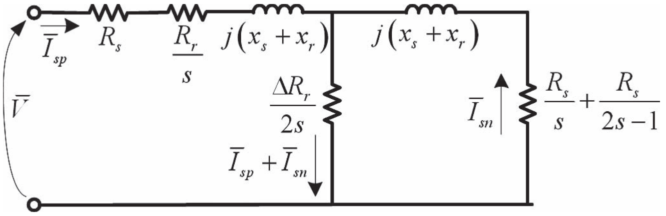

Fig. 2. Simplified equivalent circuit corresponding to system (9).

This allows to visualize the machine behavior by the equivalent circuit of Fig. 1, containing four meshes with vertical branches. The branches are due respectively to the forward magnetizing current, to the rotor asymmetry, and to the backward magnetizing current.

Far from the low slip region, the forward magnetizing current can be disregarded, cutting off the first branch. The third branch, i.e., the backward magnetizing current $\overline{I}_{sn}+\overline{I}_{rn}$, can be disregarded as well. Note that this simplification leads to neglecting the contribution that this magnetizing current, or the backward flux component at pulsation $(1-2s)\omega$, gives to the torque ripple considered in the following [24].

According to the aforementioned assumptions, $\overline{I}_{sp}=-\overline{I}_{rp}$ and $\overline{I}_{sn}=-\overline{I}_{rn}$, system (8) becomes (9), and the equivalent circuit is reduced to the two-mesh circuit of Fig. 2

$$\begin{aligned}\overline{V}&=\left[R_s+\frac{R_r}{s}+j(x_s+x_r)\right]\overline{I}_{sp}+\frac{\frac{\Delta R_r}{2}}{s}(\overline{I}_{sp}+\overline{I}_{sn})\\ 0&=\left(\frac{R_s}{2s-1}+\frac{R_r}{s}+j(x_s+x_r)\right)\overline{I}_{sn}+\frac{\frac{\Delta R_r}{2}}{s}(\overline{I}_{sp}+\overline{I}_{sn}).\end{aligned} \tag{9}$$

System (9) allows to express $\overline{I}_{sn}$ as a function of $\overline{I}_{sp}$

$$\overline{I}_{sn}=\frac{\frac{\frac{\Delta R_r}{2}}{s}}{\frac{R_s}{2s-1}+\frac{R_r+\Delta R_r/2}{s}+j(x_s+x_r)}\overline{I}_{sp}. \tag{10}$$

In the denominator of (10), near the rated slip, the main parameter is R_r/s. Therefore, in case of $n=1$

$$\overline{I}_{sn}\simeq\frac{\frac{\Delta R}{2s}}{\frac{R_r}{s}}\overline{I}_{sp}=\frac{\Delta R}{2R_r}\overline{I}_{sp}=\frac{n}{N}\overline{I}_{sp}=\frac{1}{N}\overline{I}_{sp}. \tag{11}$$

Having neglected the forward magnetizing current, (11) does not hold for low slip values. A better approximation is obtained if the amplitude I_{sn} is referred to the fundamental current once the magnetizing current I_o is subtracted

$$\overline{I}_{\text{sn}}\simeq\frac{n}{N}(\overline{I}_{\text{sp}}-\overline{I}_o)=\frac{1}{N}(\overline{I}_{\text{sp}}-\overline{I}_o). \tag{12}$$

The current ratio is fairly constant in a large slip range, and this is typical of machines of various sizes [24], [41]. It can be concluded that (12) allows to diagnose the fault on a wide range of machines and operating conditions at constant speed.

There is a slight numerical discrepancy between the results obtained by (12) and machine simulations, mainly due to neglecting end-ring currents. In case of large size machines with high pole numbers, the end-ring contribution is vanishingly small, and so is the no-load current. In this case, (11) approximates well the machine behavior.

All the previous considerations on one phase current can be applied to the current space vector. In steady state, only the component I_{sn} at pulsation $(1-2s)\omega$ *or* $2s\omega$ is present, and it will be denoted as the initial (i.e., with infinite inertia) left side component $I'_l=I_{sn}$ with phase $\varphi_{I'_l}$. In the next section, we will show how it is dynamically modified by the speed ripple effect.

The current space vector $\vec{i}$ in a reference frame rotating at pulsation ω is

$$\vec{i}=\sqrt{\frac{3}{2}}\left[Ie^{-j\Phi}+I'_l e^{-j\left(2s\omega t+\varphi_{I'_l}\right)}\right]. \tag{13}$$

In addition to the dc component $\sqrt{3/2}I(\cos\Phi-j\sin\Phi)$, the fault component at pulsation $-2s\omega$ is present. The locus described by $\vec{i}$ in the active–reactive plane is a circle traveled counterclockwise with radius I'_l and center $\sqrt{3/2}[Ie^{-j\Phi}]$, corresponding to active and reactive ripple components with the same amplitude $I'_l=I_{sn}$.

The $2s\omega$ component in the current introduces a ripple component in the EM torque. The flux space vector is $\vec{\lambda}=\sqrt{3/2}[\lambda e^{-j\pi/2}]$, and the EM torque is

$$\begin{aligned}T_{\text{em}}(t)&=P\vec{\lambda}\wedge\vec{i}\\ &=\frac{3}{2}P\left[\lambda e^{-j\pi/2}\right]\wedge\left[Ie^{j(\omega t-\Phi)}+I'_l e^{j\left[(1-2s)\omega t-\varphi_{I'_l}\right]}\right]\\ &=\frac{3}{2}P\lambda I\cos\Phi+\frac{3}{2}P\lambda\left[I'_l\cos\left(2s\omega t+\varphi_{I'_l}\right)\right].\end{aligned} \tag{14}$$

The EM torque develops a new component $\Delta T'_{\text{em}}(t)$ at pulsation $2s\omega$ proportional to the $2s\omega$ component of the current

---

$$\begin{bmatrix}\bar{V}\\0\\0\\0\end{bmatrix}=\begin{bmatrix}R_s+j(X_m+x_s) & 0 & jX_m & 0\\ 0 & \frac{R_s}{2s-1}+j(X_m+x_s) & 0 & jX_m\\ jX_m & 0 & \frac{R_r}{s}+j(X_m+x_r) & \frac{\frac{\Delta R_r}{2}}{s}\\ 0 & jX_m & \frac{\frac{\Delta R_r}{2}}{s} & \frac{R_r}{s}+j(X_m+x_r)\end{bmatrix}\begin{bmatrix}\overline{I_{sp}}\\ \overline{I_{sn}}\\ \overline{I_{rp}}\\ \overline{I_{rn}}\end{bmatrix} \tag{7}$$

space vector

$$\Delta T'_{\mathrm{em}}(t) = \frac{3}{2} P \lambda \left[I'_l \cos\left(2s\omega t + \varphi_{I'_l} \right) \right]. \tag{15}$$

IV. MACHINE BEHAVIOR WITH SPEED REACTION: CURRENT SPACE VECTOR COMPONENTS AND CURRENT SIDEBAND FEATURES

With finite inertia, torque ripple generates speed ripple through the mechanical transfer function; the EM system, in turn, modifies this initial torque ripple through a feedback loop mechanism. With sufficiently high inertia, the machine response is inertial and can be modeled simply [24]. The speed ripple is linked to the actual EM torque ripple $\Delta T_{\mathrm{em}}(t)$ superimposed to the load torque by the integral relationship $\Delta\omega_r(t) = 1/J \int \Delta T_{\mathrm{em}}(t) dt$, and reference can be made to a quasi-steady state around the operating point. Speed ripple induces motional EMFs and, therefore, new current components at pulsations $(1 \pm 2s)\omega$ (or $2s\omega$ in the rotating reference frame).

According to [3], the actual left sideband component I_l is the composition of a new speed ripple caused component I''_l at $(1 - 2s)\omega$ ($-2s\omega$ in the rotating reference frame) and the initial one I'_l. Its amplitude is similar to the amplitude of the right side component I_r, but the displacement between $\overline{I''_l}$ and $\overline{I'_l}$ is unknown. In the past, the authors have hypothesized a displacement of π in order to retrieve the initial value I'_l, dependent on fault severity, through the sum of the two actual sideband amplitudes, but it was not clear in which operating conditions this hypothesis held.

A recent development enables to determine this angular displacement using a synchronous reference frame [24]. In the rotating reference frame, the current space vector is

$$\vec{i} = \sqrt{\frac{3}{2}} \left[I e^{-j\Phi} + I_l e^{-j\left(2s\omega t + \varphi_{I_l}\right)} + I_r e^{j\left(2s\omega t - \varphi_{I_r}\right)} \right]. \tag{16}$$

We determine the active and reactive components of current ripple as functions of the sideband components

$$\begin{aligned} \Delta\vec{i} &= \left[\Delta i_{\mathrm{act}}(t) - j\Delta i_{\mathrm{react}}(t)\right] \\ &= \sqrt{\frac{3}{2}} \left[I_l e^{-j(2s\omega t + \varphi_{I_l})} + I_r e^{j(2s\omega t - \varphi_{I_r})} \right] \\ &= \sqrt{\frac{3}{2}} \left[I_l \cos(2s\omega t + \varphi_{I_l}) + I_r \cos(2s\omega t - \varphi_{I_r}) \right] \\ &\quad - j\sqrt{\frac{3}{2}} \left[I_l \sin(2s\omega t + \varphi_{I_l}) - I_r \sin(2s\omega t - \varphi_{I_r}) \right]. \end{aligned} \tag{17}$$

The displacement of the two sinusoidal terms representing the real and imaginary parts of the current space vector at pulsation $2s\omega$ is easily computed by the envelope of the sinusoidal functions obtained projecting the demodulated current space vector on the synchronous reference frame.

Moving from the time-varying representation to the phasor representation, the following phasors can be defined:

$$\overline{I}_l = I_l e^{-j\varphi_{I_l}}, \; \overline{I}_r = I_r e^{j\varphi_{Ir}}, \; \overline{\Delta I}_{\mathrm{act}} = \Delta I_{\mathrm{act}} e^{j\varphi_{I_{\mathrm{act}}}},$$

$$\overline{\Delta I}_{\mathrm{react}} = \Delta I_{\mathrm{react}} e^{j\varphi_{I_{\mathrm{react}}}}.$$

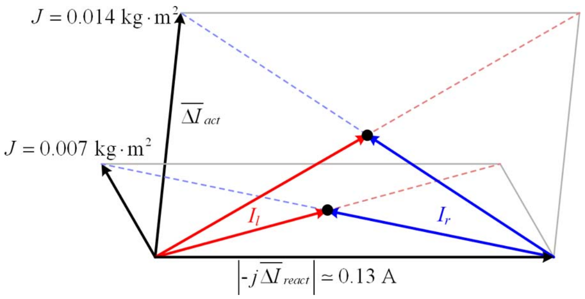

Fig. 3. Derivation of $\overline{I_l}$ and $\overline{I_r}$ from the sum and difference of the phasors $-j\overline{\Delta I}_{\mathrm{react}}$ and $\overline{\Delta I}_{\mathrm{act}}$ for two inertia values.

Then, using (17)

$$\overline{\Delta I}_{\mathrm{act}} = \overline{I}_l + \overline{I}_r, \quad \overline{\Delta I}_{\mathrm{react}} = j\overline{I}_l - j\overline{I}_r \tag{18}$$

and therefore, it is possible to compute the current sideband phasors from the active and reactive space vector components

$$\overline{I}_l = \frac{\overline{\Delta I}_{\mathrm{act}} - j\overline{\Delta I}_{\mathrm{react}}}{2}, \quad \overline{I}_r = \frac{\overline{\Delta I}_{\mathrm{act}} + j\overline{\Delta I}_{\mathrm{react}}}{2}. \tag{19}$$

The phasor angles are revealing, enabling a thorough comprehension of physical phenomena involving torque and speed ripple, as will be shown in Section V.

The shapes of the involved physical quantities have been explored through extensive simulations of different machines in different load and inertia conditions with a low dissymmetry (one broken bar) as justified in Section II. The simulations reported below are referred to a machine with a nameplate 1.5-kW 230-V 50-Hz die cast rotor with $N = 28$ bars, $P = 2$ pole pairs at full load, and one broken bar. Different load conditions and different machines have been considered as well, and the results can be found in [24] and [41].

Varying the inertia, it results that the amplitude ΔI_{act}, starting from the initial value I'_l (for $J \to \infty$), decreases strongly with decreasing inertia, while $\Delta I_{\mathrm{react}}$, starting from I'_l as well, remains fairly constant. The computation of $\overline{I_l}$ and $\overline{I_r}$ according to (19) can be visualized as in Fig. 3 where the phasor $\overline{\Delta I}_{\mathrm{act}}$ is reported for two inertia values. $\overline{I}_l$ and $\overline{I}_r$ are the semidiagonals of the parallelogram formed by $-j\overline{\Delta I}_{\mathrm{react}}$ and $\overline{\Delta I}_{\mathrm{act}}$, respectively. This construction shows clearly the machine reaction to speed ripple: A right side current component is produced that decreases the initial left side component, being

$$\overline{I_l} = \overline{I'_l} + \overline{I_r}. \tag{20}$$

The different current components and their displacements are reported in Figs. 4 and 5. Some experimental results, obtained according to the procedure described in Section VI, are reported in the figures as well.

As it can be seen, the displacement angle between $\overline{I}_l$ and $\overline{I}_r$ depends heavily on inertia, emphasizing that the sum of the amplitudes of $\overline{I}_l$ and $\overline{I}_r$ used for diagnostic aims [3]–[8] is not always effective. In particular, such diagnostic technique works well only for very low values of inertia, typically around the intrinsic rotor inertia. Which fault signature can be used outside this very limited field?

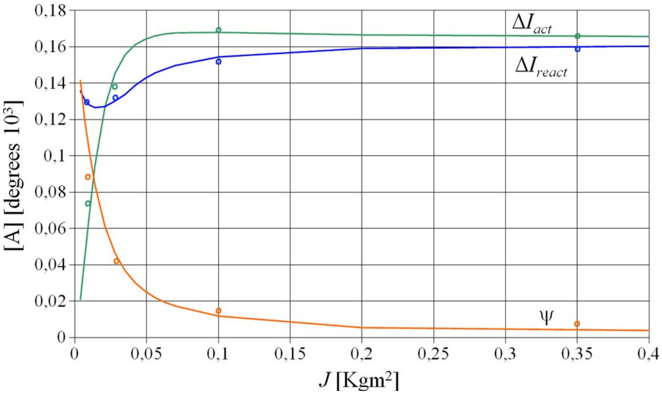

Fig. 4. Shapes of peak values of $\overline{\Delta I}_{\mathrm{act}}, \overline{\Delta I}_{\mathrm{react}}$ and phase displacement ψ of $\overline{\Delta I}_{\mathrm{act}}$ over $-j\overline{\Delta I}_{\mathrm{react}}$ versus inertia from simulation. Points from experiments.

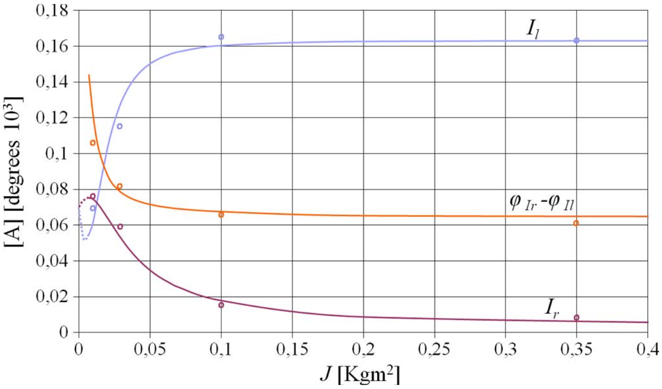

Fig. 5. Shapes of peak values of $\overline{I}_l, \overline{I}_r$ and their angular displacement versus inertia from simulation. Points from experiments.

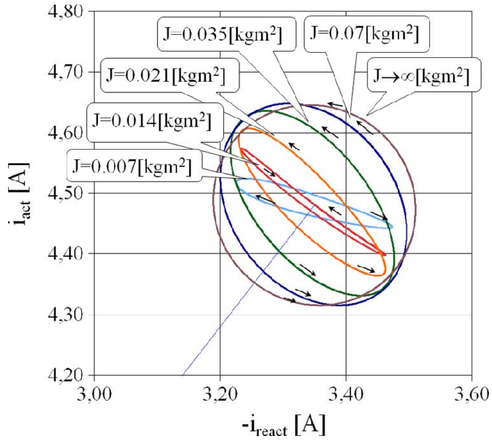

Fig. 6. Enlargement around the operating point of the current space vector $\vec{i}(t)$ for different inertia values.

If the locus of the current space vector is considered, the circle found in steady state becomes an ellipse, whose projection on the imaginary axis, equal to $\overline{\Delta I}_{\mathrm{react}} = \Delta I_{\mathrm{react}} e^{j\varphi_{I_{\mathrm{react}}}}$, is fairly constant with inertia and can be a better indicator of fault severity than the sum of the left and right sideband amplitudes.

Fig. 6 reports the current space vector loci for different values of inertia.

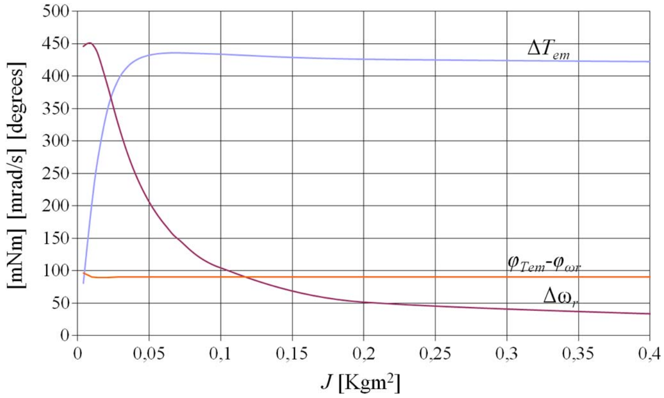

Fig. 7. Torque and speed ripple and their angular displacement versus inertia from simulation.

The EM torque component $\Delta T_{\mathrm{em}}(t)$ at pulsation $2s\omega$ becomes

$$\begin{aligned}\Delta T_{\mathrm{em}}(t) &= \frac{3}{2}P\lambda\left[I_l\cos\left(2s\omega t + \varphi_{I_l}\right) + I_r\cos\left(2s\omega t - \varphi_{I_r}\right)\right]\\ &= \sqrt{\frac{3}{2}}P\lambda\Delta i_{\mathrm{act}}(t).\end{aligned} \tag{21}$$

The representative phasor for the EM torque at pulsation $2s\omega$ (21) can be introduced as well, and this allows to visualize the torque ripple variation with inertia according to the variation of $\overline{\Delta I}_{\mathrm{act}}$ or $\overline{I}_l + \overline{I}_r$

$$\overline{\Delta T}_{\mathrm{em}} = \frac{3}{2}P\lambda\overline{\Delta I}_{\mathrm{act}} = \frac{3}{2}P\lambda(\overline{I}_l + \overline{I}_r). \tag{22}$$

The shapes of torque ripple, speed ripple, and their displacements are reported in Fig. 7. Note the similar shapes of ΔT_{em} and ΔI_{act} in Figs. 7 and 4, respectively, and of $\Delta\omega_r$ and I_r in Figs. 7 and 5, respectively.

V. LOCI OF CURRENT COMPONENTS AND EQUIVALENT CIRCUIT WITH VARYING INERTIA

The simulations show, besides a constant value of $\overline{\Delta I}_{\mathrm{react}}$, a constant value of the angle β between $\overline{\Delta I}_{\mathrm{act}}$ and $\overline{I}_r$: This feature allows a geometrical interpretation of how the phasors change with inertia. The vertex of the parallelogram formed by $-j\overline{\Delta I}_{\mathrm{react}}$ and $\overline{\Delta I}_{\mathrm{act}}$, with the phasor $2\overline{I}_r$ as a diagonal, describes a circle, with $-j\overline{\Delta I}_{\mathrm{react}}$ as the chord which subtends an equal inscribed angle. The vertices of $\overline{\Delta I}_{\mathrm{act}}$ and $2\overline{I}_r$ move along this circle with changing inertia. The constant value of their angular displacement is fundamental and will be analytically justified in the following. For the machine under test at full load and with one broken bar, this angle results in $\beta = 54^\circ$.

Fig. 8 shows the loci and the phasors referred to inertia values of 0.07, 0.014, and 0.007 $\mathrm{kg} \cdot \mathrm{m}^2$. At infinite inertia, $-j\overline{\Delta I}_{\mathrm{react}}$ and $\overline{\Delta I}_{\mathrm{act}}$ overlap, the vertex of $\overline{\Delta I}_{\mathrm{act}}$ is in B, and $\overline{I}_r$ is zero. Decreasing the inertia, the vertex moves along the circle, and with inertia approaching zero, the vertex approaches point A. The particular nonmonotonic shapes of I_l and I_r at low inertia, obtained also in [42], are perfectly justified.

The aforementioned geometrical representation suggests that the fault signature to be used at large values of inertia, when

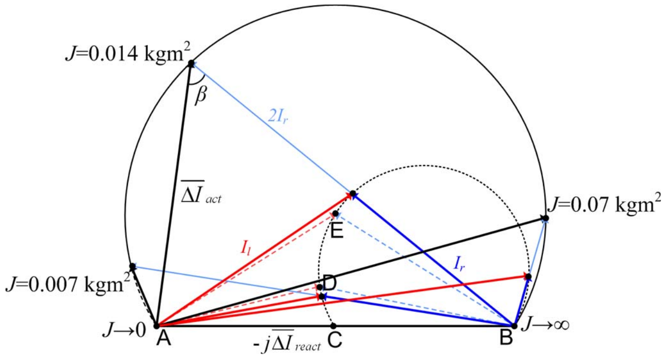

Fig. 8. Loci described by $\overline{\Delta I}_{\text{act}}$ and $2\overline{I}_r$ assuming $-j\overline{\Delta I}_{\text{react}}$ as reference with $0 < J < \infty$.

the sum of the sidebands is no longer effective, is ΔI_{react}. The initial left sideband amplitude I_l' is well approximated by ΔI_{react}, which is fairly independent of inertia.

There is a second circle, described by the vertex of $\overline{I_l}$ and $\overline{I_r}$, to be noted (dotted circle in Fig. 8). When inertia approaches zero, this vertex tends to point C, corresponding to equal lengths of $\overline{I_l}$ and $\overline{I_r}$.

We now follow the physical cause/effect chain with the help of Fig. 8 in order to understand the machine behavior and the origin of the constant value of β. The machine reaction modifies the initial torque ripple $\overline{\Delta T}'_{\text{em}}$ so that (22), from the geometrical construction in Fig. 8, can be written as

$$\overline{\Delta T}_{\text{em}} = \frac{3}{2} P\lambda \left(\overline{I}_l' + 2\overline{I}_r\right) = \frac{3}{2} P\lambda (\overline{\Delta I}_{\text{react}} + 2\overline{I}_r). \quad (23)$$

The total torque decrease is therefore linked to twice the right sideband component amplitude. Using phasor representation, the relationships among the different variables become

$$\overline{\Delta\omega}_r = -j\frac{\overline{\Delta T}_{\text{em}}}{J 2s\omega} \quad (24)$$

for speed and torque ripple and

$$\overline{\Delta\theta} = -\frac{1}{2s\omega} j\overline{\Delta\omega}_r = -\frac{1}{J(2s\omega)^2}\overline{\Delta T}_{\text{em}} \quad (25)$$

for the consequent mechanical angular variation. Simulations agree with the results obtained by (24) and (25).

The mechanical angle variation acts on the stator flux space vector. Applying Taylor's series truncated to the second term, its effect can be modeled as the addition of a time-varying term to the fundamental stator flux

$$\begin{aligned}\overline{\lambda}(t) &= \sqrt{\frac{3}{2}}\lambda e^{-j(\pi/2 - P\Delta\theta(t))} = -j\sqrt{\frac{3}{2}}\lambda e^{jP\Delta\theta(t)}\\ &\simeq -j\sqrt{\frac{3}{2}}\lambda[1 + jP\Delta\theta(t)] = -j\sqrt{\frac{3}{2}}\lambda + \sqrt{\frac{3}{2}}\lambda P\Delta\theta(t). \quad (26)\end{aligned}$$

Using phasors, the new flux component at pulsation $2s\omega$ is $\overline{\Delta\lambda} = \lambda P\overline{\Delta\theta}$. This motional flux at pulsation $2s\omega$ is added to the existing transformer flux, which allows the transfer of the rotor backward current component due to the asymmetry to the stator.

So far, we considered the origin of the fault-generated speed ripple. Let us now apply the effects of this speed ripple (a time-varying flux and, consequently, a fault-induced EMF) to the machine in order to study the electrical reaction. The EMF is a small signal superimposed to the applied voltage, producing small effects on the fundamental variables. The further effects of such disturbance on machine asymmetries are second order, and the machine can thus be assumed symmetrical.

The fault-induced EMF can be modeled as a voltage source which, inserted in the symmetrical machine, produces a current reaction. The Park machine model of the symmetrical machine in the supply pulsation reference frame is [35]

$$\begin{aligned}&\begin{bmatrix}(p + j\omega)\Delta\lambda\\ 0\end{bmatrix}\\ &= \begin{bmatrix}R_s + (p + j\omega)L_s & (p + j\omega)M\\ [p + j(\omega - P\omega_r)]\,M & R_r + [p + j(\omega - P\omega_r)]\,L_r\end{bmatrix} \cdot \begin{bmatrix}i_{\text{stat}}\\ i_{\text{rot}}\end{bmatrix}\end{aligned} \quad (27)$$

where i_{stat} and i_{rot} are the stator and rotor currents. Using phasors, the Laplace operator $p = d/dt$ applied to variables at pulsation $2s\omega$ can be replaced by $j2s\omega$; ,therefore $d/dt + j\omega$ is replaced by $j(1 + 2s)\omega$, while $d/dt + j(\omega - P\omega_r)$ is replaced by $3s\omega$. The system becomes

$$\begin{bmatrix}j(1 + 2s)\lambda P\overline{\Delta\theta}\\ 0\end{bmatrix} = \begin{bmatrix}R_s + j(1 + 2s)\omega L_s & j(1 + 2s)\omega M\\ j3s\omega M & R_r + j3s\omega L_r\end{bmatrix} \cdot \begin{bmatrix}\overline{I}_{\text{stat}}\\ \overline{I}_{\text{rot}}\end{bmatrix}. \quad (28)$$

The equations can be referred to a same pulsation ω dividing the first one by $(1 + 2s)$ and dividing the second by $3s$, and the second equation, system (29), is obtained

$$\begin{bmatrix}j\lambda P\overline{\Delta\theta}\\ 0\end{bmatrix} = \begin{bmatrix}\frac{R_s}{1+2s} + j\omega L_s & j\omega M\\ j\omega M & \frac{R_r}{3s} + j\omega L_r\end{bmatrix} \cdot \begin{bmatrix}\overline{I}_{\text{stat}}\\ \overline{I}_{\text{rot}}\end{bmatrix}. \quad (29)$$

Obviously, this mathematical passage alters the current pulsations: $\overline{I}_{\text{stat}}$ goes from $(1 + 2s)\omega$ to ω, and $\overline{I}_{\text{rot}}$ goes from pulsation $3s\omega$ to ω, both with unchanged amplitude.

It is useful to highlight the forward magnetizing current $(\overline{I}_{\text{stat}} + \overline{I}_{\text{rot}})$

$$\begin{aligned}j\lambda P\overline{\Delta\theta} &= \left[\frac{R_s}{(1 + 2s)} + j\omega l_s\right]\overline{I}_{\text{stat}} + j\omega M(\overline{I}_{\text{stat}} + \overline{I}_{\text{rot}})\\ 0 &= j\omega M(\overline{I}_{\text{stat}} + \overline{I}_{\text{rot}}) + \left[\frac{R_r}{3s} + j\omega l_r\right]\overline{I}_{\text{rot}}. \quad (30)\end{aligned}$$

System (30) allows to visualize the machine behavior by the equivalent circuit of Fig. 9. Two meshes with the stator and the rotor equivalent currents, respectively, are present, while the inner branch is due to the forward magnetizing current. The stator mesh contains the voltage source corresponding to the EMF.

Far from the low slip region, the magnetizing current can be disregarded, cutting off the magnetizing branch. The equivalent circuit is reduced to that of Fig. 10.

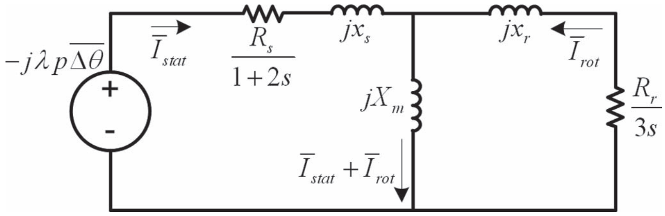

Fig. 9. Equivalent circuit corresponding to system (30).

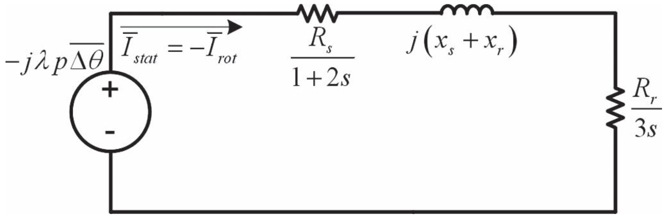

Fig. 10. Simplified equivalent circuit corresponding to (31).

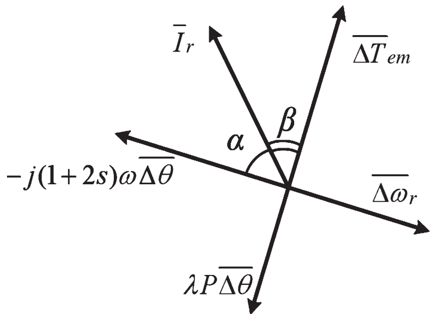

Fig. 11. Qualitative phasor diagram linking $\overline{\Delta T}_{\rm em}$ (or $\overline{\Delta I}_{\rm act}$) with $\overline{\Delta\omega}_r$, $\overline{\Delta\theta}$, and $\overline{I}_r$.

The stator current yields the right sideband, and neglecting the stator resistance, very simple relationships can be obtained

$$\overline{I}_{\rm rot}=\overline{I}_r=\frac{-j\lambda P\overline{\Delta\theta}}{\frac{R_s}{(1+2s)}+jx_s+\frac{R_r}{3s}+jx_r}\simeq\frac{-j\lambda P\overline{\Delta\theta}}{\frac{R_r}{3s}+j(x_s+x_r)}=\frac{\overline{e}}{\overline{Z}}. \tag{31}$$

The angular relationships among the phasors involved in the speed reaction to torque ripple are visualized in Fig. 11.

Starting from torque ripple $\overline{\Delta T}_{\rm em}$, speed ripple $\overline{\Delta\omega}_r$ lags by $\pi/2$, $\overline{\Delta\theta}$ again lags by $\pi/2$, the same for the EMF $-j(1+2s)\omega\lambda P\overline{\Delta\theta}$ opposite to $\overline{\Delta\omega}_r$, and then, $\overline{I}_r$ is shifted by angle α, being

$$\alpha\simeq arctg\frac{3s(x_s+x_r)}{R_r}. \tag{32}$$

This relationship shows clearly that the displacement

$$\beta=\pi-\alpha \tag{33}$$

between $\overline{I}_r$ and $\overline{\Delta T}_{\rm em}$ depends only on machine parameters and load, while it is independent of inertia. This development supports the previous observation (from both simulations and experiments) that this angle is constant for a given machine at a given load condition. For the considered 1.5-kW machine, passing from the rated slip to half, the angle β varies from 54° to 67° for the decrease of α due to the increase of the equivalent resistance $R_r/3s$ with respect to the reactance. These results are reported in [24].

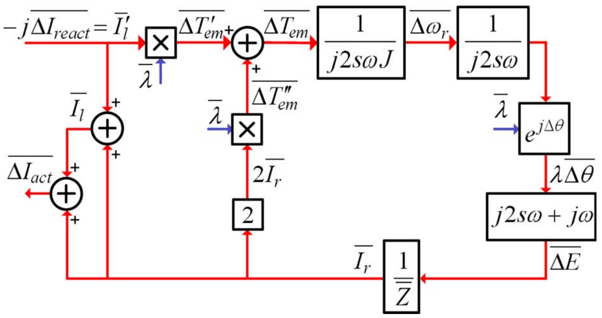

Fig. 12. Closed-loop block diagram of the faulty machine behavior.

The angle α is highly dependent on machine design. Generally, the equivalent resistance $R_r/3s$ decreases with respect to the reactance with increasing machine sizes; therefore, α increases, and β decreases. Results involving a larger test machine can be found in [41].

The cause/effect chain rotor asymmetry → torque ripple → speed ripple → machine reaction to speed ripple described earlier can be represented as a closed-loop block diagram reporting the quantities at pulsation $2s\omega$ (see Fig. 12). Although it is a very simplified representation, it helps understand the relationships among the physical quantities involved, and it justifies why angle β is constant.

VI. EXPERIMENTAL TEST BED

In order to verify the theoretical analysis on the effects of inertia, a suitable test bed, realized by the authors, was used.

The motor under test was connected to a brake test bench which included a speed-controlled permanent-magnet machine. The test bench has the capability of measuring speed, torque, voltages, and currents of the machine under test.

The permanent-magnet brake was driven through a speed control feedback loop with a proportional gain K_P^ω and no integral action. The speed control loop constrains the speed ripple due to the rotor fault (which, to the control loop, is an external disturbance), realizing a virtual increase of the inertia. This strategy allows a continuous variation of the inertia attached to the tested machine without the need to physically swap weights and flanges.

At twice the slip pulsation $2s\omega$, i.e., torque ripple pulsation, the virtual inertia is proportional to the proportional gain [43]

$$J_v=\frac{K_TK_P^\omega}{(2s\omega)}. \tag{34}$$

The results of experiments at different values of equivalent inertia are reported in Figs. 4 and 5. The measurements are in fair agreement with the simulation results. The discrepancies can be ascribed to the assumptions of the model and to the presence of unavoidable intrinsic rotor asymmetries that influence the tests.

VII. CONCLUSION

This paper presented a representation of the behavior of faulty rotor induction machines which allows a deep physical understanding of the phenomena involved. A faulty machine model was first used to derive a fault-induced EMF due to speed ripple. Then, such disturbance was introduced in a healthy machine model in order to close the physical cause/effect loop chain.

Extensive simulations, confirmed by experiments, showed how the behavior of the fault-affected physical quantities depends on inertia, allowing insightful geometrical representations of the variables involved.

The analytical model confirms the experimental observations and shows that, through the active and reactive components of current ripple and the use of phasors, it is possible to improve the usual MCSA technique based on the sum of the current sideband amplitudes, used to quantify the severity of rotor bar breakage.

REFERENCES

[1] A. Bellini, F. Filippetti, C. Tassoni, and G.-A. Capolino, “Advances in diagnostic techniques for induction machines,” *IEEE Trans. Ind. Electron.*, vol. 55, no. 12, pp. 4109–4126, Dec. 2008.

[2] B. G. Hargis, K. Gaydon, and K. Kamash, “The Detection of Rotor Defects in Induction Motors,” in *Proc. IEE Elect. Mach., Design Appl. Conf.*, London, U.K., 1982, pp. 216–220.

[3] F. Filippetti, G. Franceschini, C. Tassoni, and P. Vas, “AI techniques in induction machines diagnosis including the speed ripple effect,” *IEEE Trans Ind. Appl.*, vol. 34, no. 1, pp. 98–108, Jan./Feb. 1998.

[4] W. T. Thomson and M. Fenger, “Case histories of current signature analysis to detect faults in induction motor drives,” in *Proc. IEEE IEMDC*, Madison, WI, Jun. 2003, pp. 1459–1465.

[5] A. Bellini, F. Filippetti, G. Franceschini, C. Tassoni, and G. B. Kliman, “Quantitative evaluation of induction motor broken bars by means of electrical signature analysis,” *IEEE Trans. Ind. Appl.*, vol. 37, no. 5, pp. 1248–1255, Sep./Oct. 2001.

[6] S. M. A. Cruz and A. J. M. Cardoso, “Multiple reference frames theory: A new method for the diagnosis of stator faults in three-phase induction motors,” *IEEE Trans. Energy Convers.*, vol. 20, no. 3, pp. 611–619, Sep. 2005.

[7] I. M. Culbert and W. Rhodes, “Using current signature analysis technology to reliably detect cage winding defects in squirrel-cage induction motors,” *IEEE Trans. Ind. Appl.*, vol. 43, no. 2, pp. 422–428, Mar./Apr. 2007.

[8] B. Xu, L. Sun, and H. Ren, “A new criterion for the quantification of broken rotor bars in induction motors,” *IEEE Trans. Energy Convers.*, vol. 25, no. 1, pp. 100–106, Mar. 2010.

[9] G. Didier, E. Ternisien, O. Casparyu, and H. Razik, “Fault detection of broken rotor bars in induction motors using a global flux index,” *IEEE Trans. Ind. Appl.*, vol. 42, no. 1, pp. 79–88, Jan./Feb. 2006.

[10] M. Blodt, J. Faucher, B. Dagues, and M. Chabert, “Mechanical load fault detection in induction motors by stator current time frequency analysis,” *IEEE Trans. Ind. Appl.*, vol. 42, no. 6, pp. 1454–1463, Nov. 2006.

[11] I. Jaks and P. Fuchs, “Demodulation analysis for exact rotor fault detection under changing parameters,” in *Proc. IEEE SDEMPED*, Cargèse, France, Sep. 2009, pp. 1–7.

[12] H. Jin, N. Faliang, and Y. Jiaqiang, “Induction motor rotor fault diagnosis method based on double PQ transformation,” *Front. Elect. Electron. Eng. China*, vol. 2, no. 1, pp. 117–122, Mar. 2007.

[13] V. Choqueuse, M. E. H. Benbouzid, Y. Amirat, and S. Turri, “Diagnosis of three-phase electrical machines using multidimensional demodulation techniques,” *IEEE Trans. Ind. Electron.*, vol. 59, no. 4, pp. 2014–2023, Apr. 2012.

[14] A. D. Silva, R. Povinelli, and N. Demerdash, “Induction machine broken bars and short circuit diagnostics based on three phase stator current envelopes,” *IEEE Trans. Ind. Electron.*, vol. 55, no. 3, pp. 1310–1318, Mar. 2008.

[15] H. Arabacı and O. Bilgin, “Diagnosis of broken rotor bar faults by using frequency spectrum of stator current envelope,” in *Proc. ICEM*, Marseille, France, Sep. 2–5, 2012, pp. 1643–1646.

[16] C. Kral, F. Pirker, and G. Pascoli, “The impact of inertia on rotor fault effects—Theoretical aspects of the vienna monitoring method,” *IEEE Trans. Power Electron.*, vol. 23, no. 4, pp. 2136–2142, Jul. 2008.

[17] M. Trzynadlowski and E. Ritchie, “Comparative investigation of diagnostic media for induction motors: A case of rotor cage faults,” *IEEE Trans. Ind. Electron.*, vol. 47, no. 5, pp. 1092–1099, Oct. 2000.

[18] Z. Liu, X. Yin, Z. Zhang, D. Chen, and W. Chen, “Online rotor mixed fault diagnosis way based on spectrum analysis of instantaneous power in squirrel cage induction motors,” *IEEE Trans. Energy Convers.*, vol. 19, no. 3, pp. 485–490, Sep. 2004.

[19] M. Drif and A. J. M. Cardoso, “The instantaneous reactive power approach for rotor cage fault diagnosis in induction motor drives,” in *Proc. IEEE PESC*, Rhodes, Greece, Jun. 2008, pp. 1548–1552.

[20] M. Eltabach, J. Antoni, G. Shanina, and X. Carniel, “Broken rotor bars detection by a new non-invasive diagnostic procedure,” *Mech. Syst. Signal Process.*, vol. 23, no. 4, pp. 1398–1412, May 2009.

[21] M. Entalbach, A. Charara, and I. Zein, “A comparison of external and internal method of signal spectra analysis for broken bar detection in induction motors,” *IEEE Trans. Ind. Electron.*, vol. 51, no. 1, pp. 107–121, Feb. 2004.

[22] H. De Angelo, G. R. Bossio, and G. O. Garcia, “Discriminating broken rotor bar from oscillating load effects using the instantaneous active and reactive powers,” *IET Elect. Power Appl.*, vol. 4, no. 4, pp. 281–290, Apr. 2010.

[23] G. R. Bossio, C. H. De Angelo, C. M. Pezzani, J. M. Bossio, and G. O. Garcia, “Separating broken rotor bars and load oscillations on IM fault diagnosis through instantaneous active and reactive current,” *IEEE Trans. Ind. Electron.*, vol. 56, no. 11, pp. 4571–4580, Nov. 2009.

[24] C. Concari, G. Franceschini, and C. Tassoni, “A new method to discern mechanical unbalances from rotor faults in induction machines,” in *Proc. IEEE ICEM*, Jul. 2012, pp. 310–321.

[25] A. Ceban, R. Pusca, and R. Romary, “Study of rotor faults in induction motors using external magnetic field analysis,” *IEEE Trans. Ind. Electron.*, vol. 59, no. 5, pp. 2082–2093, May 2012.

[26] G. A. Capolino and H. Henao, “A new model for three-phase induction machine diagnosis using a simplified spectral approach,” in *Conf. Rec. IEEE IAS Annu. Meeting*, Chicago, IL, Oct. 2001, vol. 3, pp. 1558–1563.

[27] A. R. Munoz and T. A. Lipo, “Complex vector model of the squirrel-cage induction machine including instantaneous rotor bar currents,” *IEEE Trans. Ind. Appl.*, vol. 35, no. 6, pp. 1332–1340, Nov./Dec. 1999.

[28] H. A. Toliyat and T. A. Lipo, “Transient analysis of cage induction machines under stator, rotor bar and end ring faults,” *IEEE Trans. Energy Convers.*, vol. 10, no. 2, pp. 241–247, Jun. 1995.

[29] B. Liang, B. S. Payne, A. D. Ball, and S. D. Iwnicki, “Simulation and fault detection of three-phase induction motors,” *Math. Comput. Simul.*, vol. 61, no. 1, pp. 1–15, Nov. 2002.

[30] H. Henao, C. Martis, and G.-A. Capolino, “An equivalent internal circuit of the induction machine for advanced spectral analysis,” *IEEE Trans. Ind. Appl.*, vol. 40, no. 3, pp. 726–734, May/Jun. 2004.

[31] H. Henao, A. Razik, and G.-A. Capolino, “Analytical approach of the stator current frequency harmonics computation for detection of induction machines rotor fault,” *IEEE Trans. Ind. Appl.*, vol. 41, no. 3, pp. 801–807, May/Jun. 2005.

[32] A. Khezzar, M. Hadjami, N. Bessous, M. E. K. Oumaamar, and H. Razik, “Accurate modelling of cage induction machine with analytical evaluation of inductances,” in *Proc. IEEE IECON*, Orlando, FL, Oct. 2008, pp. 1112–1117.

[33] B. Mirafzal, R. J. Povinelli, and N. A. O. Demerdash, “Effect of load magnitude on diagnosing broken bar faults in induction motors using the pendulous oscillation of the rotor magnetic orientation,” *IEEE Trans. Ind. Appl.*, vol. 41, no. 3, pp. 771–783, May/Jun. 2005.

[34] P. Vas, F. Filippetti, G. Franceschini, and C. Tassoni, “Transient modelling oriented to diagnostics of induction machines with rotor asymmetry,” in *Proc. ICEM*, Paris, France, Sep. 1994, pp. 62–67.

[35] G. J. Retter, *Matrix And Space Phasor Theory Of Electric Machines*. Budapest, Hungary: Akadémiai Kiadó, 1987.

[36] T. J. Sobczyk and W. Maciolek, “Asymmetry factors of induction motor rotor cages,” in *Proc. IEEE SDEMPED*, Grado, Italy, Sep. 2001, pp. 487–491.

[37] C. Kral, “Derivation of the space phasor equation and the required parameters of a squirrel cage induction machine with a faulty rotor bar,” in *Proc. IEEE SDEMPED*, Goijon, Spain, Sep. 1999, pp. 395–400.

[38] M. Stockes, F. Rodyukof, and A. Medvedev, “Idealized two-axis model of induction machines under rotor faults,” in *Proc. IEEE ICIEA*, Singapore, May 2006, pp. 1–7.

[39] K. Drobonic, M. Nemec, D. Makuc, R. Fiser, and V. Ambrozic, “Pseudo-salient model of induction motor with broken bars,” in *Proc. IEEE SDEMPED*, Bologna, Italy, Sep. 2011, pp. 1–6.

[40] S. M. A. Cruz and F. Gaspar, “A new PQ method to diagnose rotor faults in three phase induction motors coupled to time-varying loads,” in *Proc. IEEE SDEMPED*, Bologna, Italy, Sep. 2011, pp. 1–7.

[41] C. Concari, G. Franceschini, and C. Tassoni, “An insightful geometrical interpretation of spectral components of the physical quantities involved in induction machines rotor faults,” in *Proc. IEEE SDEMPED*, Bologna, Italy, Sep. 2011, pp. 24–30.

[42] G. R. Bossio, C. H. De Angelo, C. M. Pezzani, J. M. Bossio, and G. O. Garcia, “Evaluation of harmonic current sidebands for broken bar diagnosis in induction motors,” in *Proc. IEEE SDEMPED*, Cargèse, France, Sep. 2009, pp. 1–6.

[43] A. Bellini, C. Concari, G. Franceschini, E. Lorenzani, C. Tassoni, and A. Toscani, “Virtual inertia test bed for quantification of sideband currents in induction machines diagnostics,” in *Proc. ICEM*, Kania, Greece, Sep. 2006, pp. 1–6.

Carlo Concari (S’98–M’06) was born in San Secondo Parmense, Italy, in 1976. He received the M.S. degree in electronics engineering and the Ph.D. degree in information technology from the University of Parma, Parma, Italy, in 2002 and 2006, respectively.

Since 2006, he has been an Assistant Professor with the Department of Information Engineering, University of Parma. His research activity is mainly focused on power electronics, digital drive control, static power converters, and electric machine diagnostics.

Giovanni Franceschini was born in Reggio Emilia, Italy, in 1960. He received the M.S. degree in electronic engineering from the University of Bologna, Bologna, Italy.

Since 1990, he has been with the Department of Information Engineering, University of Parma, Parma, Italy, where he was first an Assistant Professor and is currently a Full Professor of electric machines and drives. He is the author or coauthor of more than 150 technical papers and is the holder of four industrial patents. His research interests include high-performance electric drives and diagnostic techniques for industrial electric systems.

Carla Tassoni (SM’97) was born in Bologna, Italy, in 1942. She received the M.S. degree in electrical engineering from the University of Bologna, Bologna, in 1966.

She joined the University of Bologna as an Assistant Professor, later becoming an Associate Professor of Electrical Machines in the Department of Electric Engineering. She is currently a Full Professor of Electrical Engineering with the University of Parma, Parma, Italy. She is the author or coauthor of more than 150 scientific papers. Her main research interests include simulation and modeling of electric systems and applications of diagnostic techniques.

Andrea Toscani was born in Fidenza, Italy, in 1976. He received the M.S. degree in electronic engineering and the Ph.D. degree in information technology from the University of Parma, Parma, Italy, in 2004 and 2008, respectively.

Since May 2004, he has been with the Department of Information Engineering, University of Parma. His research activity is mainly focused on power electronics, drive control, and diagnostics.